The Astrophysical Journal, 850:145 (17pp), 2017 December 1 https://doi.org/10.3847/1538-4357/aa961a

Boxy Orbital Structures in Rotating Bar Models

L. Chaves-Velasquez[1], P. A. Patsis[2], I. Puerari[1], Ch. Skokos[3], and T. Manos[4,5,6]
[1] Instituto Nacional de Astrofísica, Óptica y Electrónica, Calle Luis Enrique Erro 1, 72840 Santa María Tonantzintla, Puebla, Mexico; leonardochaves83@gmail.com
[2] Research Center for Astronomy, Academy of Athens, Soranou Efessiou 4, GR-115 27 Athens, Greece
[3] Department of Mathematics and Applied Mathematics, University of Cape Town, Rondebosch, 7701, South Africa
[4] CAMTP—Center for Applied Mathematics and Theoretical Physics, University of Maribor, Krekova 2, SI-2000 Maribor, Slovenia
[5] School of Applied Sciences, University of Nova Gorica, Vipavska 11c, SI-5270 Ajdovščina, Slovenia
[6] Institute of Neuroscience and Medicine, Brain and Behaviour (INM-7), Research Centre Jülich, Jülich, Germany
Received 2017 June 6; revised 2017 October 6; accepted 2017 October 20; published 2017 November 28

Abstract

We investigate regular and chaotic two-dimensional (2D) and three-dimensional (3D) orbits of stars in models of a galactic potential consisting of a disk, a halo, and a bar to find the origin of boxy components that are part of the bar or (almost) the bar itself. Our models originate in snapshots of an *N*-body simulation, which develops a strong bar. We consider three snapshots of the simulation, and, for the orbital study, we treat each snapshot independently, as an autonomous Hamiltonian system. The calculated corotation–to–bar length ratios indicate that in all three cases, the bar rotates slowly, while the orientation of the orbits of the main family of periodic orbits changes along its characteristic. We characterize the orbits as regular, sticky, or chaotic after integrating them for a 10 Gyr period by using the $GALI_2$ index. Boxiness in the equatorial plane is associated either with quasi-periodic orbits in the outer parts of stability islands or with sticky orbits around them, which can be found in a large range of energies. We indicate the location of such orbits in diagrams, which include the characteristic of the main family. They are always found about the transition region from order to chaos. By perturbing such orbits in the vertical direction, we find a class of 3D nonperiodic orbits, which have boxy projections both in their face-on and side-on views.

Key words: chaos – galaxy: kinematics and dynamics – galaxy: structure

1. Introduction

Strong bars are observed in optical images of almost half of all nearby disk galaxies (see, e.g., Marinova & Jogee 2007; Reese et al. 2007; Barazza et al. 2008).This percentage increases to nearly 70% when near-infrared images are considered (Eskridge et al. 2000; Knapen et al. 2000; Menéndez-Delmestre et al. 2007). Bars are characterized by three parameters: length, strength, and pattern speed. This last parameter is defined as the rotational frequency of the bar and determines to a large extent the dynamics of a barred galaxy. Bars are classified as fast or slow by means of the ratio $R = R_{\rm CR}/a_b$, where $R_{\rm CR}$ is the corotation radius and a_b is the length of the semimajor axis of the bar. The orbital theory shows that bars cannot extend beyond corotation (Contopoulos 1980). In the case of fast rotators, we have $1.0 < R < 1.4$, while for slow rotators, $R > 1.4$ (Athanassoula 1992b; Debattista & Sellwood 2000). By definition, in a slow rotator, corotation is located far from the end of the bar.

Structures in barred galaxies have to be supported by stellar orbits (Contopoulos 2002; Binney & Tremaine 2008). It is now known that not only regular but also chaotic sticky orbits can be used for building the bars (Wozniak 1994; Kaufmann & Contopoulos 1996; Patsis et al. 1997; Wozniak & Pfenniger 1999; Muzzio et al. 2005; Harsoula & Kalapotharakos 2009; Harsoula et al. 2010; Patsis et al. 2010; Contopoulos & Harsoula 2013; Patsis & Katsanikas 2014b; Tsigaridi & Patsis 2015). Sticky orbits are chaotic orbits that wander for relatively long times close to the outer borders of stability islands before eventually entering a well-defined chaotic region in the system's phase space. In some other cases, there is also stickiness near unstable asymptotic curves in the chaotic sea, which is called "stickiness in chaos" (Contopoulos & Harsoula 2008). In both cases, sticky orbits mimic the behavior of quasi-periodic orbits in the configuration space during the time they remain confined in a region of phase space. However, ultimately, during their time evolution, they will exhibit a change in their orbital morphology, as they will at a certain time change their behavior from quasi-regular to completely chaotic.

Special features and deviations from the standard orbital dynamics (Contopoulos & Grosbol 1989) have been encountered in several cases. For example, in Tsigaridi & Patsis (2015), the orbital stellar dynamics of a two-dimensional (2D), slowly rotating, barred-spiral model has been investigated. In this case, orbital families have been presented that support in the galactic plane an inner ring and an X feature embedded in the bar. However, the dynamics associated with this model is different from that of a typical bar ending close to corotation. The ring was a result of a folding of the characteristic ("S" shape), along which the orientation of the elliptical orbits of the main family and their stability vary (bistable bifurcation). Furthermore, the observed boxiness and the X feature reflected the presence of sticky orbits at energy levels corresponding to the middle of the barred-spiral potential. Folding of the characteristic curve of the main planar family was found earlier in the work of Skokos et al. (2002b) in the case of a three-dimensional (3D) bar again rotating slowly. Questions that arise are how common is this feature in the backbone families of real bars, and what are the implications for the observed morphologies?

The aim of this work is to study the underlying dynamics in three analytic models that have a common origin, being derived from snapshots of an *N*-body simulation reported in Machado & Athanassoula (2010). We want to examine the degree of chaoticity of the bar-supporting orbits. In that simulation, the interaction between the dark matter halo and the disk develops a bar, which evolves in time. We consider for our study three snapshots at times 4.2, 7, and 11.2 Gyr. Each snapshot is modeled by a frozen potential, so we treat each one of them as

Table 1
The Parameters of the Models Fitting the Snapshots of the *N*-body Simulation of MM

	Bar					Disk			Halo			
s/s	Time (Gyr)	a (kpc)	b (kpc)	c (kpc)	Ω_b (km s^{-1} kpc^{-1})	M_B ($10^{10}M_\odot$)	A (kpc)	B (kpc)	M_D ($10^{10}M_\odot$)	a_H (kpc)	γ	M_H ($10^{10}M_\odot$)
1	1.4	2.24	0.71	0.44	52	1.04	1.92	0.22	3.96	3.90	0.23	25
2	4.2	5.40	1.76	1.13	24	2.36	0.95	0.53	2.64	5.21	0.71	25
3	7.0	7.15	2.38	1.58	14	3.02	0.78	0.56	1.98	5.77	0.85	25
4	11.2	7.98	2.76	1.93	9	3.30	0.71	0.59	1.70	5.95	0.89	25

Notes. Successively, we give the number of the snapshot (s/s), the time of the snapshot, the semi-axes of the Ferrers bar (a, b, c), the pattern speed of the bar Ω_b, the mass of the bar M_B, the scale lengths of the Miyamoto disk A and B, the disk mass M_D, the scale radius of the halo a_H, the dimensionless parameter γ in the Dehnen halo potential, and the mass of the halo M_H (units as in MM).

a time-independent model; i.e., we use in our work the formalism for autonomous Hamiltonian systems. The bar is modeled with a Ferrers potential (Ferrers 1877), the disk is a Miyamoto–Nagai disk (Miyamoto & Nagai 1975), and the dark matter halo is a Dehnen potential (Dehnen 1993). The models for these snapshots have been taken from Manos & Machado (2014, hereafter MM). Throughout the text, by referring to a "snapshot," we will refer to the corresponding model in MM.

In particular, we want to examine the relation between the morphological features of the bars and the degree of chaos of the orbits that support these features. Such features include a possible inner and/or outer boxiness of the bar and the formation of rings. In the 3D barred models in Patsis & Katsanikas (2014a, 2014b), it has been suggested that inner boxy features can be built by means of quasi-periodic orbits at the edges of the stability islands of the x1 family, as well as with sticky orbits just beyond the last invariant torus around the stable x1 periodic orbit. It has also been proposed that such orbits support boxiness both in face-on and edge-on projections at the central region of the bar (about halfway to the end of the bar). A similar dynamical phenomenon led to the boxy features on the galactic plane in the bars of 2D barred-spiral models in Tsigaridi & Patsis (2015).

In the present study, we want to investigate what kind of orbits support double boxy morphologies in the successive snapshots, and how they evolve in time, i.e., from the model of the earlier snapshot to the model for the final one. We want to examine whether this dynamical mechanism is associated with orbits just beyond the vertical 2:1 resonance region or can be applied in a large energy range in which we can find bar-supporting orbits. For this purpose, we do not investigate in detail the structure of phase space in a large number of energies, but we investigate the systems' global dynamics using chaos indicators.

Many techniques have been developed over the years for determining the regular or chaotic nature of the orbits of dynamical systems. Review presentations of some of the most commonly used methods can be found in Skokos et al. (2016). Among these chaos indicators, the Smaller Alignment Index (SALI) method (Skokos 2001; Skokos et al. 2003, 2004) and its extension, the Generalized Alignment Index (GALI) technique (Skokos et al. 2007, 2008; Manos et al. 2012), proved to be quite efficient in revealing the chaotic nature of orbits of Hamiltonian systems in a fast and accurate way. The computation of these indices is based on the time evolution of more than one deviation vector from the studied orbits. The SALI/GALI methods have already been successfully applied to dynamical studies of astronomical problems (see, e.g., Sándor et al. 2004; Capuzzo-Dolcetta et al. 2007; Soulis et al. 2007; Voglis et al. 2007; Manos et al. 2008; Voyatzis 2008; Bountis & Papadakis 2009; Harsoula & Kalapotharakos 2009; Manos & Athanassoula 2011; Manos et al. 2013; Carpintero et al. 2014; Machado & Manos 2016). The reader is referred to Skokos & Manos (2016) for a recent review of the theory and applications of the SALI/GALI chaos indicators.

In order to study the degree of chaoticity of the orbits of our models, we use the $GALI_2$ index, whose time evolution reveals quite efficiently the regular, sticky, or chaotic nature of the studied orbit. It can also tell the time interval within which a sticky orbit behaves as a regular one, being able this way to support a given morphological structure. For these reasons, the use of $GALI_2$ is an essential tool for the needs of our investigation. We also note here that the $GALI_2$ index is closely related to the SALI method (see, for example, Appendix B of Skokos et al. 2007).

The paper is organized as follows. In Section 2, we explain the gravitational potentials that model the components of the *N*-body snapshots. In Section 3, we present the numerical methods used in our study. In particular, we introduce the Hamiltonian of the system. The $GALI_2$ index is introduced as well. In Section 4, we present the results of our study. We describe the characteristic curves of the main planar family of periodic orbits in the models we study, and we label the initial conditions of the integrated nonperiodic orbits according to the degree of their chaoticity. Finally, in Section 5, we summarize our findings and present and discuss our conclusions.

2. Modeling the *N*-body Snapshots

In our study, we closely follow the approach of the work of MM. The models used for approximating the morphologies encountered in the studied snapshots of the *N*-body simulation consist of a bar embedded in an axisymmetric disk and halo environment. The bar is represented by a Ferrers model (Ferrers 1877), the disk is a typical Miyamoto–Nagai model (Miyamoto & Nagai 1975), and the spherical dark matter halo surrounding the disk is represented by a Dehnen potential (Dehnen 1993). The mathematical formulae for these potentials can be found in MM.

The structural and dynamical parameters of the bar, disk, and halo of the models are adopted from the models in MM and summarized in Table 1. In this table, we include an earlier snapshot presented in MM at $t = 1.4$ Gyr, which, however, has not yet developed a strong bar. We keep it in the table, but we will not present any orbital analysis for its small bar. Thus, the

Table 2
Parameters Associated with the Pattern Speed of the Studied Models

snapshot 2	$t = 4.25$ Gyr	$R_{L_1} = 10.83$	$R = 2.0$
snapshot 3	$t = 7.00$ Gyr	$R_{L_1} = 16.46$	$R = 2.3$
snapshot 4	$t = 11.2$ Gyr	$R_{L_1} = 22.88$	$R = 2.87$

Note. Each row successively gives the name of the snapshot, the time after the beginning of the simulation that it is taken, the radius of the Lagrangian point L_1, and the corotation–to–bar length ratio.

models in Table 1 correspond to four snapshots taken at times $t = 1.4$ Gyr, $t = 4.2$ Gyr, $t = 7.0$ Gyr, and $t = 11.2$ Gyr. We name them snapshot 1, 2, 3, and 4, respectively.

The scaling of the units we used in our calculations, which also corresponds to the numbers that appear in the axes of the figures in this work, are: 1 kpc (length), $2 \times 10^{11} M_{\odot}$ (mass), and 1 kpc^2 Myr^{-2} (energy), while $G = 1$.

Having the parameters of each model available, we consider the length of the bar to be the length of the semimajor axis of the Ferrers bar, a. Also, from the pattern speed of each model, Ω_b, we compute the location of the Lagrangian points L_1 and L_2. We consider the corotation radius to be their distance from the center of the system. Then, we calculate the ratio $R = R_{\rm CR}/a_b = R_{L_1}/a$. For the three models we analyzed, the values we found are given in Table 2.

We note that the R_{L_4} values are very close to the R_{L_1} ones, being 10.75, 16.37, and 22.89, respectively. We realize that in all cases, $R > 1.4$, which places all models in the class of slow rotators.

3. Autonomous Hamiltonian System and the GALI$_2$ Index

The Hamiltonian of the system is given by

$$H = \frac{1}{2}(p_x^2 + p_y^2 + p_z^2) + \Phi(x, y, z) - \Omega_b(xp_y - yp_x) = E_J, \quad (1)$$

where x, y, z are Cartesian coordinates, p_x, p_y, p_z are the conjugate momenta in the inertial reference frame, and Ω_b is the pattern speed of the bar. In addition, E_J is the energy of Jacobi and $\Phi = \Phi_B + \Phi_D + \Phi_H$, where Φ_B is the potential of the bar, Φ_D is the potential of the disk, and Φ_H is the potential of the halo.

The equations of motion and the variational equations we use in order to follow the evolution of the two deviation vectors from the studied orbit can be found in the MM paper. They are needed for computing the GALI$_2$ index. The GALI$_2$ index is given by the absolute value of the wedge product of two normalized-to-unity deviation vectors $\hat{\boldsymbol{w}}_1(t)$ and $\hat{\boldsymbol{w}}_2(t)$:

$$\mathrm{GALI}_2(t) = |\hat{\boldsymbol{w}}_1(t) \wedge \hat{\boldsymbol{w}}_2(t)| \quad (2)$$

(see MM for details).

Thus, in order to evaluate GALI$_2$, we integrate the equations of motion and the variational equations for two deviation vectors simultaneously. The GALI$_2$ index behaves as follows (see Skokos & Manos 2016 and references therein):

1. For chaotic orbits, it falls exponentially to zero as
$$\mathrm{GALI}_2(t) \propto \exp(-(\lambda_1 - \lambda_2)t), \quad (3)$$
where λ_1 and λ_2 are the two largest Lyapunov exponents (for the computation of the Lyapunov exponents, see Benettin et al. 1980; Skokos 2010).
2. For regular orbits, it oscillates around a positive value across the integration:
$$\mathrm{GALI}_2(t) \propto \text{constant}. \quad (4)$$
3. In the case of sticky orbits, we observe a transition from practically constant GALI$_2$ values, which correspond to the seemingly quasi-periodic epoch of the orbit, to an exponential decay to zero, which indicates the orbit's transition to chaoticity.

4. The Degree of Chaoticity of the Orbits

4.1. Planar Orbits

In a rotating Ferrers bar, the elliptical periodic orbits of the main families are characterized by a single nonzero initial condition along the minor axis of the bar, namely their position along the y-axis in our models. The curve of zero velocity (ZVC) in a (E_J, y_0) diagram separates the region where orbital motion is allowed from the region where it is not. Since the main family consists of direct periodic orbits, only the $y_0 > 0$ part of such a diagram is of interest for us. An (E_J, y_0) diagram is the projection of a complete (E_J, y_0, p_{y_0}) figure with all possible initial conditions. However, it is sufficient for describing the properties of the orbits we present below. The line that gives the y_0 initial condition of the main family of periodic orbits is the characteristic curve of the model. Since we want to study chaoticity in a large range of energies, we have created such (E_J, y_0) diagrams for the potentials of the three snapshots we study. In order to calculate the degree of chaoticity of the planar orbits around the main family of periodic orbit as we move from the center of the system toward corotation, we use the GALI$_2$ index. We have used the GALI$_2$ index to color-code each point in the allowed region in the (E_J, y_0) areas. The shade of the color[7] indicates the GALI$_2$ index that a given orbit, i.e., a point in the (E_J, y_0) diagram, has at the end of the integration. In other words, the color of an (E_J, y_0) point indicates if the orbit with y_0 initial condition at E_J will lead to regular (large $\log_{10}$(GALI$_2$) values) or chaotic (very small $\log_{10}$(GALI$_2$) values) motion. At the borders between these regions, we find points with intermediate $\log_{10}$(GALI$_2$) values, which correspond to sticky chaotic orbits.

4.1.1. Snapshot 2, $t = 4.2$ Gyr

For each model, we sample the GALI$_2$ index at two time windows: after time t_1, corresponding to 1 Gyr, and after time t_2, corresponding to 10 Gyr. In this way, we investigate both the relatively short-term and the long-term behavior of the orbits. The two color-coded (E_J, y_0) diagrams for snapshot 2 are given in Figure 1. Figure 1(a) gives the index after $t_1 = 1$ Gyr, and Figure 1(b) gives it after $t_2 = 10$ Gyr.

Darker shades indicate more chaotic orbits. The color for each orbit is determined according to its $\log_{10}$(GALI$_2$) value and is taken from the color bars given on the right-hand side of the panels.

In Figure 1 and all similar subsequent figures, the curve of zero velocity is indicated with "ZVC." As determined by Equation (1), motion is allowed only to the right of the ZVC, as

[7] In the electronic version of the paper, we use shades of blue to color-code the orbits. However, in the printed version, the corresponding figures are given in shades of gray.

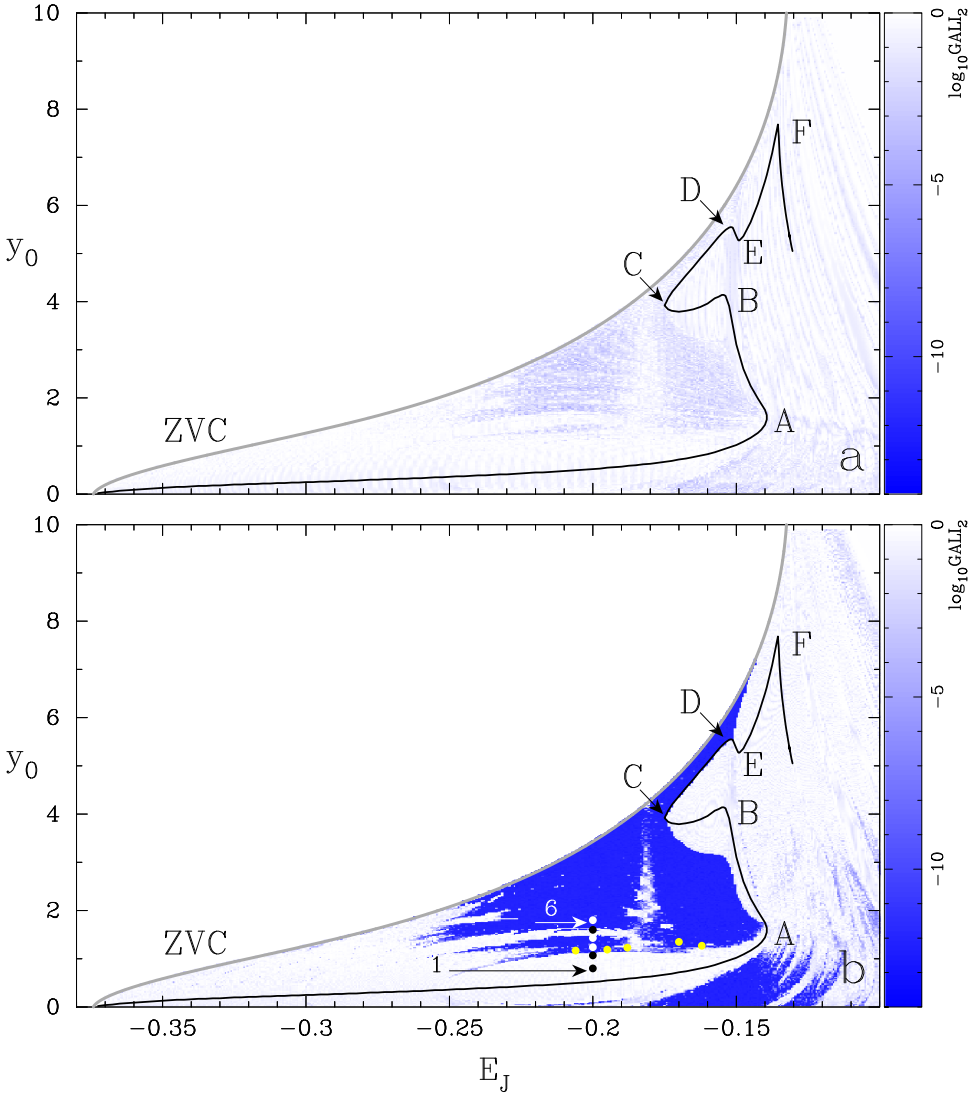

Figure 1. The chaoticity of the planar orbits on the equatorial plane of snapshot 2 is given in color-coded (E_J, y_0) diagrams. The color of each orbit (each point in the figure) corresponds to the value of the $\log_{10}(GALI_2)$ quantity calculated for it and is taken from the color bars on the right-hand side of the figure. In panel (a), we calculate $\log_{10}(GALI_2)$ for $t_1 = 1$ Gyr, while in panel (b), we calculate it for $t_2 = 10$ Gyr. In both panels, the zero-velocity curve is indicated with "ZVC." The solid black line in the region where motion is allowed is the characteristic of the main family. Capital letters (A, B, . . . F) and arrows pointing to points C and D are used for facilitating the description of the evolution of the curve in the text. We observe that, in general, the orbits with the smaller $GALI_2$ index in panel (a), which reach values $\log_{10}(GALI_2) \lessapprox -5$, become strongly chaotic in panel (b). However, panel (b) also shows additional features indicating chaotic behavior that are absent in panel (a). Such features are the dark blue tails above the characteristic for $-0.27 \lessapprox E_J \lessapprox -0.17$. The six solid dots at $E_J = -0.2$ indicate the initial conditions of the orbits we use to demonstrate the relation between $GALI_2$ and their morphology in Figure 3. Arrows point to the first and sixth of them. The five solid, light gray (yellow in the online version) dots at $E_J = -0.206$, -0.195, -0.18798, -0.17, and -0.162 indicate the initial conditions of the boxy orbits we present in Figure 4.

drawn in Figure 1. The local E_J maximum of the ZVC to the right of the figure gives the location of the Lagrangian point L_4. The solid black curve in the region where motion is allowed is the characteristic of the main family of periodic orbits. We observe that it does not grow monotonically from the center toward corotation, but after reaching point A at $E_J \approx -0.139$, it turns backward toward lower energies. After reaching a local maximum in point B, it again changes direction at $E_J \approx -0.175$, building a conspicuous open loop in the energy range $-0.175 \lessapprox E_J \lessapprox -0.152$. The loop becomes evident by following points B, C, D, and E. The turning back of the characteristic of the main family resembles the one encountered in the 2D model in Tsigaridi & Patsis (2015), as well as the one of model A2 in Skokos et al. (2002b). The joining of x1-, x2-, and x3-like morphologies in a single continuous characteristic was called by Contopoulos & Grosbol (1989) a "type 4 gap."

Following the morphological evolution of the periodic orbits along this characteristic, we realize that along its lower branch, for $E_J \lessapprox -0.139$, as well as between A and B, i.e., from $E_J \approx -0.139$ to $E_J \approx -0.155$, they are elliptical, extending along the bar. However, only the orbits with $E_J \approx -0.139$ match the size of the bar of the model. Between A and B, we find ellipses larger than the bar, as indicated in Figure 1 of MM. This means that such orbits are not populated in the model. Then, along the open loop, the ellipticity of the orbits decreases. They become circular and then again elliptical, but this time extending along the minor axis of the bar; i.e., they are x2-like. For $E_J \gtrapprox -0.152$, the periodic orbits of the main

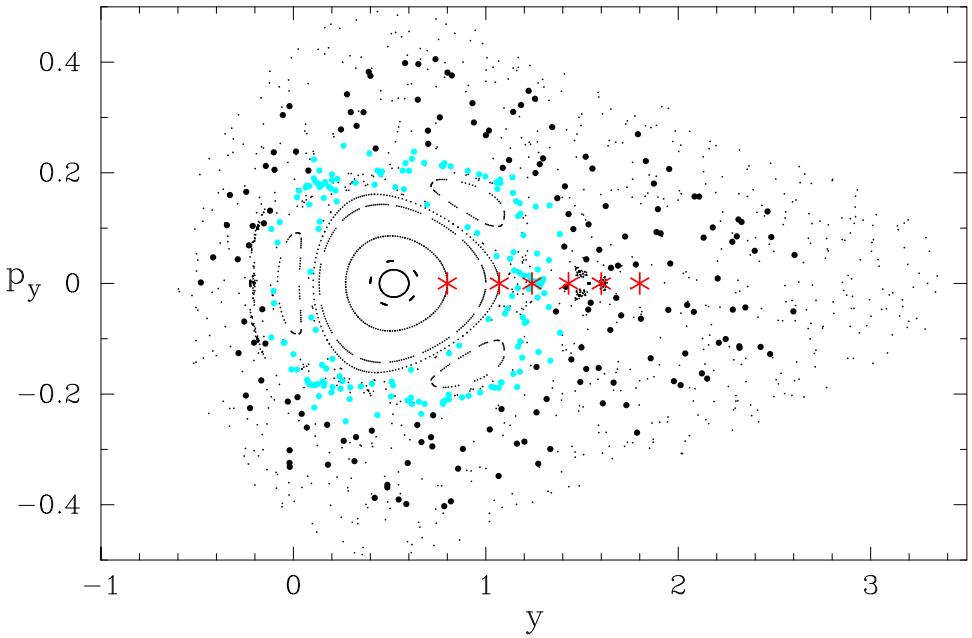

Figure 2. Poincaré surface of the section of model 2 for $E_J = -0.2$. The stable periodic orbit at $(y, p_y) \approx (0.5, 0)$ belongs to the main family of planar periodic orbits of the system. The six asterisks indicate the initial conditions of the orbits labeled 1 to 6 in Figure 1(b).

family are almost circular. We do not include in Figure 1 the characteristics of n: 1—resonance families with $n \geqslant 4$ beyond the gap at the radial 4:1 resonance. In this paper, we are interested in orbits supporting boxiness, and the bar-supporting orbits close to corotation are practically planar (Skokos et al. 2002b) with circular projections on the equatorial plane.

In Figure 1(a), color characterizes the chaoticity of the orbits after integrating them for $t_1 = 1$ Gyr. Within this time, it is expected that not only regular but also weakly chaotic, sticky orbits will retain a regular character. Such orbits will be able to support a given structure during this time period. Keeping the same scale in the colored bars on the right-hand side of the figures, we can compare the evolution of the chaotic character of the orbits from Figures 1(a) to (b). The same shade indicates the same degree of chaoticity in the two figures.

Figure 1(b) gives the same information, with the only difference being that the time of integration is $t_2 = 10$ Gyr. There is an overall similarity between the two figures. The orbits with the smaller $GALI_2$ values in Figure 1(a) (light blue areas) developed a clear chaotic character within t_2 (dark blue areas in Figure 1(b)). We also observe that there is a white stripe surrounding the characteristic of the main family for almost all energies in both figures. This indicates that the periodic orbits of the main family are stable, and thus small perturbations of their initial conditions lead to regular motion characterized by large $\log_{10}(GALI_2)$. A notable exception is the region between the CD part of the characteristic and the ZVC in Figure 1(b). A very thin dark layer also exists just below this part of the characteristic. We recall that along the same characteristic curve of the main family of our models, we encounter morphologies of periodic orbits that correspond to the stable families x1 and x2 but also to the unstable x3 family. In other models, these three families have disconnected characteristics (see, e.g., Contopoulos & Grosbol 1989; Athanassoula 1992a; Patsis & Katsanikas 2014a). We also observe that in Figure 1(b), there are clearly developed dark blue tails with chaotic orbits, absent in Figure 1(a), in the region above the characteristic of the main family for $-0.27 \lessapprox E_J \lessapprox -0.17$. Another conspicuous white zone extends almost perpendicular to the E_j axis at about $E_J \approx -0.18$. It shrinks when we integrate the orbits for $t_2 = 10$ Gyr (Figure 1(b)).

We now consider orbits along a line of constant E_J in Figure 1(b) at which regular and chaotic regions alternate in order to investigate the morphology-$GALI_2$ relation. Such an energy is, for example, $E_J = -0.2$. We observe that along the $E_J = -0.2$ axis, we encounter both regular and chaotic regions, depicted as a succession of blue (chaotic) and white (regular) regions. We present the behavior of six planar orbits at this energy with initial conditions $y_0 = 0.80$, 1.07, 1.24, 1.43, 1.60, and 1.80. In all cases, $p_{y_0} = 0$ (we recall that the major axis of the bar is along the x-axis of our system). We name these orbits 1, 2, . . . 6 and denote their location in Figure 1(b) with solid dots. We use black or white dots depending on the background in order to make them as discernible as possible. Arrows point to the location of the first (1) and sixth (6) of these orbits. Moving along a line of constant energy, we obtain some of the information a Poincaré surface of section provides. $GALI_2$ reveals the succession of regular and chaotic motion along the $p_{y_0} = 0$ axis in the Poincaré section at this energy. The width of the white space on both sides of the characteristic of the main family at a given energy is associated with the size of the stability island around the stable periodic orbit. The crossing of white stripes by an axis of constant E_J corresponds to other, smaller islands of stability that exist on the surface of section $p_{y_0} = 0$.

In Figure 2, we present the Poincaré surface of section for $E_J = -0.2$. The six asterisks along the $p_{y_0} = 0$ axis with $0.8 \leqslant y \leqslant 1.8$ are, from left to right, the initial conditions of orbits 1 to 6 indicated in Figure 1(b). The evolution of the morphologies and the quantity $\log_{10}(GALI_2)$ for these orbits within $t_1 = 1$ Gyr and $t_2 = 10$ Gyr is given in Figure 3.

Orbit 1, with $y_0 = 0.8$ (the lowest initial condition indicated with "1" in Figure 1(b)), corresponds to the left asterisk in Figure 2. From its location in the surface of section, we can see that it belongs to an invariant curve on the stability island

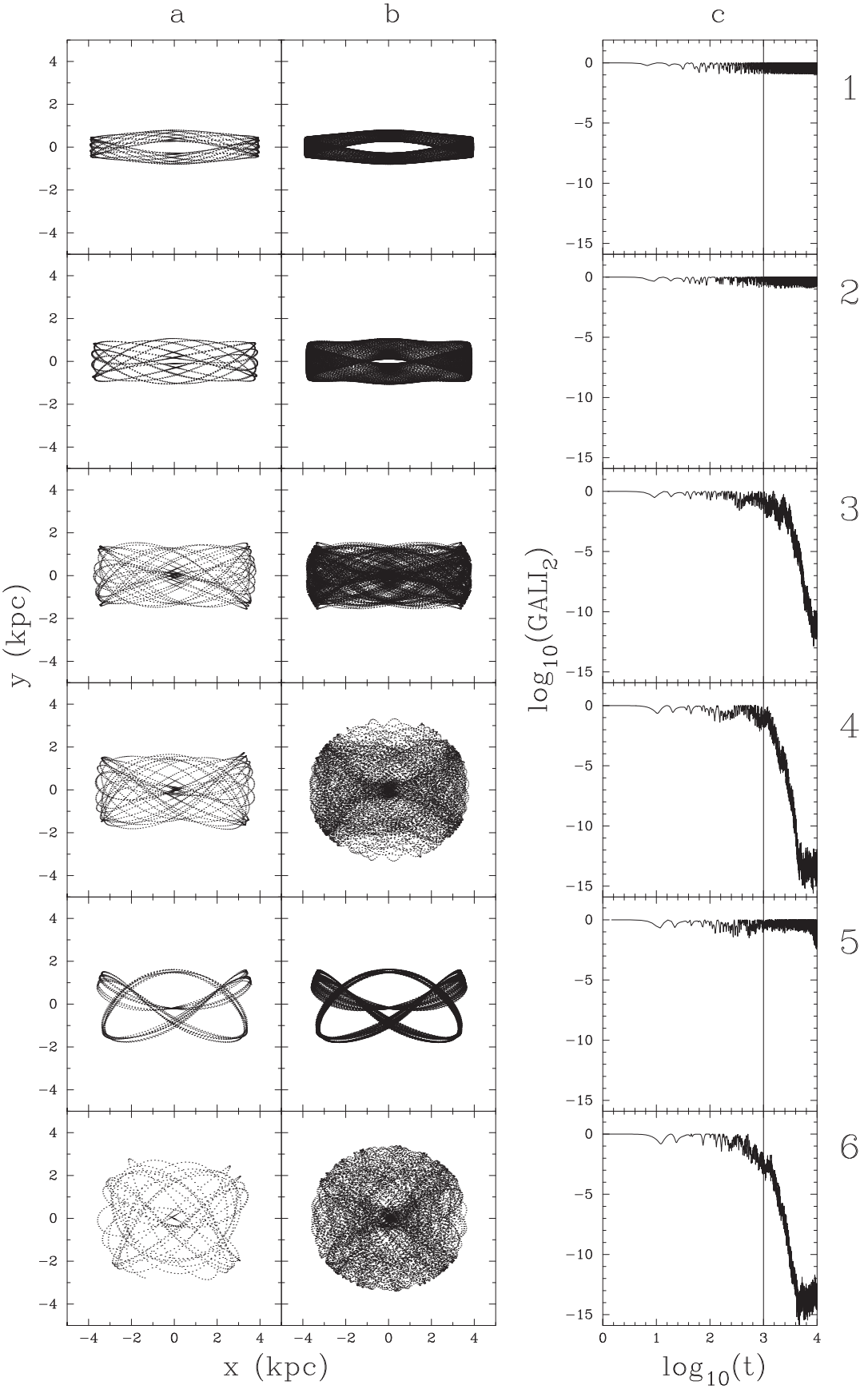

Figure 3. Six orbits with initial conditions indicated in Figure 1(b) (1 to 6) and Figure 2 (asterisks). Each row refers to the orbit mentioned on its right-hand side. The columns show (a) the morphology of the orbit within $t_1 = 1$ Gyr, (b) the morphology of the orbit within $t_2 = 10$ Gyr, and (c) the evolution of $\log_{10}(\mathrm{GALI}_2)$ within $t_2 = 10$ Gyr. The vertical line indicates the location of the first Gyr.

around the stable representative of the main family of periodic orbits and close to it. At this energy, the stable periodic orbit is a typical x1 ellipse. The quasi-periodic orbit we study has a morphology that can be vaguely described as a "thick" ellipse (panels (a) and (b) in the first row in Figure 3). Since it is a regular orbit, $\log_{10}(GALI_2)$ fluctuates close to 0 (panel (c) in the first row), as expected.

Orbit 2 has $y_0 = 1.07$ and also belongs to an invariant curve. The invariant curve around orbit 2 is very close to the last Kolmogorov–Arnold–Moser (KAM) curve (see, e.g., Contopoulos 2002) of the main stability island of Figure 2. As we observe in panel (c) of the second row of Figure 3, in this case, $\log_{10}(GALI_2)$ fluctuates close to 0. The morphology of the orbit is boxy (panels (a) and (b) for orbit 2). However, we observe that even after an integration time that corresponds to 10 Gyr, there is a central region that is not visited by the orbit.

The next orbit, 3 (with $y_0 = 1.24$), gives the gray (light blue in the online version), heavy consequents in Figure 2. For most of the integration time, these consequents are trapped around three stability islands located just beyond the invariant curve of orbit 2. However, close to the end of the integration time, orbit 3 starts diffusing in the larger chaotic sea surrounding the region with the stability islands. Thus, it is a typical sticky orbit. The quantity $\log_{10}(GALI_2)$ is very close to 0 during the first Gyr, reaching -1 close to the end of this time period (cf. the location of the vertical line in panel (c) in the third row of Figure 3). Beyond that time and up to 10 Gyr, it clearly decreases, revealing the chaotic character of the orbit (panel (c) in the third row). The morphology of the orbit is boxy for both 1 and 10 Gyr (panels (a) and (b) in the third row). Diffusion in configuration space is observed only during the time the consequents start visiting all the available space in the surface of the section. However, in Figure 2, we see that the light blue dots remain confined in a specific region. In panel (a), we observe that we have the formation of an X feature inside the box. The feature also exists in panel (b) of the third row. We find that an orbit sticky to the stability island of an x1 periodic orbit has a boxy morphology with an X embedded in it. Thus, we have in this case the formation of a boxy orbit supporting an X feature on the galactic plane by means of the dynamical mechanism described by Tsigaridi & Patsis (2015).

The orbit with $y_0 = 1.43$ (fourth asterisk from left in Figure 2) starts in the chaotic sea. Its consequents are shown with solid black dots in the surface of section. We observe that they are distributed in a larger region than the consequents of orbit 3, while they almost do not visit the region occupied by the light blue/gray consequents. For 1 Gyr, it also supports a boxy bar with an X feature as orbit 3 (panel (a) in the fourth row of Figure 3) and a rather regular behavior with $\log_{10}(GALI_2)$ close to 0 (panel (c), before the vertical line for "4"). However, for a larger time, $\log_{10}(GALI_2)$ decreases abruptly, reaching smaller values than in the case of orbit 3 (cf. panel (c) in the third and fourth rows) and, contrary to orbit 3, has a chaotic morphology (panel (b) in "4"). We also observe that for orbit 3, after 10 Gyr, $\log_{10}(GALI_2 \approx -12)$, while this happens already at $t \approx 5000$ for orbit 4.

Moving along the $p_y = 0$ axis toward larger y in Figure 2, we enter a zone occupied by barely discernible stability islands. Without going into details for the periodic orbits we find there, we just mention that in the region there is a periodic orbit of multiplicity 6. This region corresponds to the white stripe below the arrow labeled "6" in Figure 1(b). Orbit 5 ($y_0 = 1.6$) is almost on the invariant curves of the 6-ple orbit. The $\log_{10}(GALI_2)$ index points to a regular orbit (panel (c) in the fifth row of Figure 3), which is in agreement with the morphologies after 1 and 10 Gyr, as we can observe in panels (a) and (b) in "5," respectively. Actually, this is also a sticky orbit whose chaotic nature will be revealed for $t > 10$ Gyr, as toward the end of the integration, we can observe a gradual decrease of the $\log_{10}(GALI_2)$ quantity.

Finally, starting with $y_0 = 1.8$ (orbit 6), we find a chaotic orbit (scattered small dots in Figure 2). The morphologies in panels (a) and (b) in the sixth row of Figure 3 and the corresponding $\log_{10}(GALI_2)$ index (panel (c)) are in agreement with the chaotic nature of the orbit.

As we observe in column (a) of Figure 3, within $t_1 = 1$ Gyr, orbits 1 to 5 evidently support some structure. Only orbit 6 has a well-developed chaotic character. For larger time, $t_2 = 10$ Gyr, besides orbit 6, orbit 4 also has a chaotic morphology (panel (b) in the fourth and sixth rows in Figure 3). The boxy orbital structures that we are looking for are not encountered in all structure-supporting orbits. The regular orbits 1 and, essentially, 5 belong to invariant curves close to the initial conditions of the periodic orbits, and their morphology reflects to a large extent the morphology of the periodic orbits. Clear boxiness appears in orbits 2 and 3. They are located in the outermost parts of the stability island of the main periodic orbit (orbit 2) and in the sticky region around it (orbit 3), respectively, as we can observe in Figure 2. Their regular and sticky behavior is also reflected in their $\log_{10}(GALI_2)$ index within $t_2 = 10$ Gyr (panel (c) of the second and third rows in Figure 3). The chaotic orbit 4 has a morphology similar to orbit 3 only during the first Gyr of integration. This result is in agreement with the result of Tsigaridi & Patsis (2015), namely that boxiness in face-on views of bars at a given energy is introduced by orbits at the critical area close to the last KAM curve around the stable x1 orbit. They can be on either the regular or the sticky side. In the latter case, we also have the appearance of an embedded X feature.

In order to demonstrate the relation between the boxiness of the orbits and their location close to the borderline between order and chaos, we considered five more orbits in this zone at various energies. These are the orbits presented in Figure 4.

All of them are sticky, located inside the dark area but close to the borderline between white and dark (blue in the online version) regions in Figure 1(b). They are indicated with solid light gray (yellow in the online version) dots at the energies $E_J = -0.206$, -0.195, -0.18798, -0.17, and -0.162. Their initial y_0 values are, respectively, 1.17, 1.19, 1.23, 1.35, and 1.27 (always with $p_{y_0} = 0$). In Figure 4, we give them successively from left to right with increasing energy. Below each panel with the orbit in the (x,y) plane we give its $\log_{10}(GALI_2)$ index. As $GALI_2$ shows, all five orbits manifest their chaotic nature at times larger than 1 Gyr (indicated in the lower panels with a vertical line). Orbits in Figure 4(a) to (d) remain confined in the configuration space until the end of the integration time, i.e., for 10 Gyr. The orbit in Figure 4(e), at the largest energy, is more chaotic. It reaches a smaller $\log_{10}(GALI_2)$ value at time 10 Gyr, while close to the end of its integration time, it starts exploring larger regions in the configuration space. However, it also has a boxy morphology within time corresponding to about 1 Gyr.

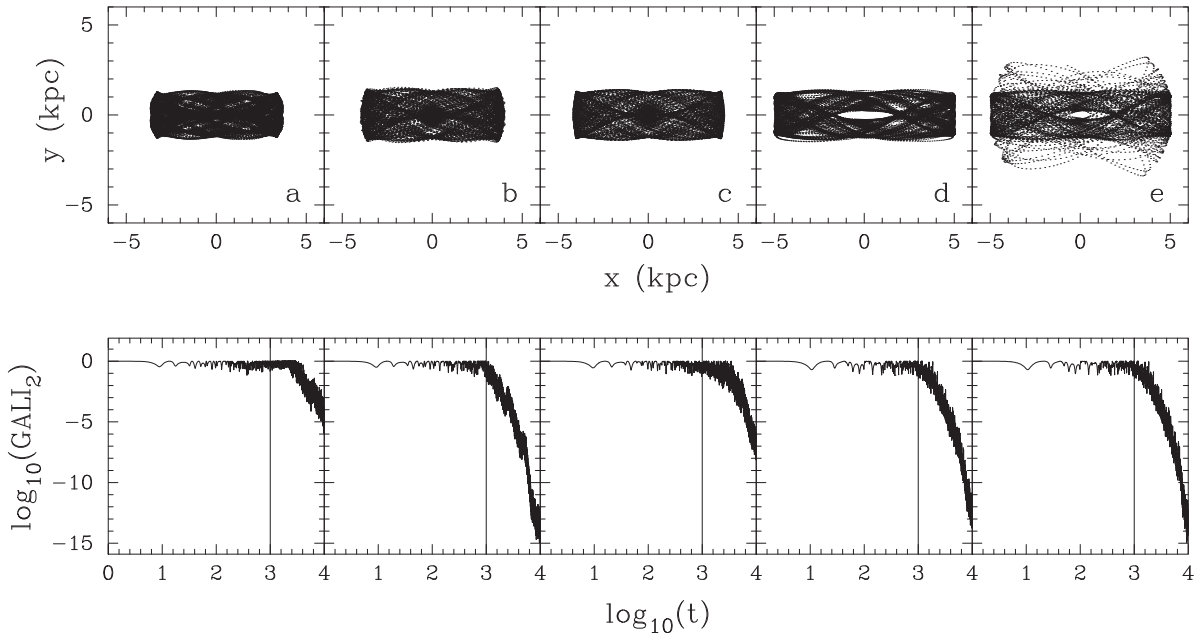

Figure 4. Five orbits with boxy character on the equatorial plane of the model of snapshot 2. Their location on the (E_J, y_0) diagram is denoted with solid light gray (yellow in the online version) dots in Figure 1(b). They are (a) (−0.206, 1.17), (b) (−0.195, 1.19), (c) (−0.18798, 1.23), (d) (−0.17, 1.35), and (e) (−0.162, 1.27). All of them are sticky to the stability islands of the stable representative of the main family of periodic orbits of the system. Below each panel of the first row is given the corresponding $GALI_2$ index up to 10 Gyr. The vertical line indicates the location of the first Gyr.

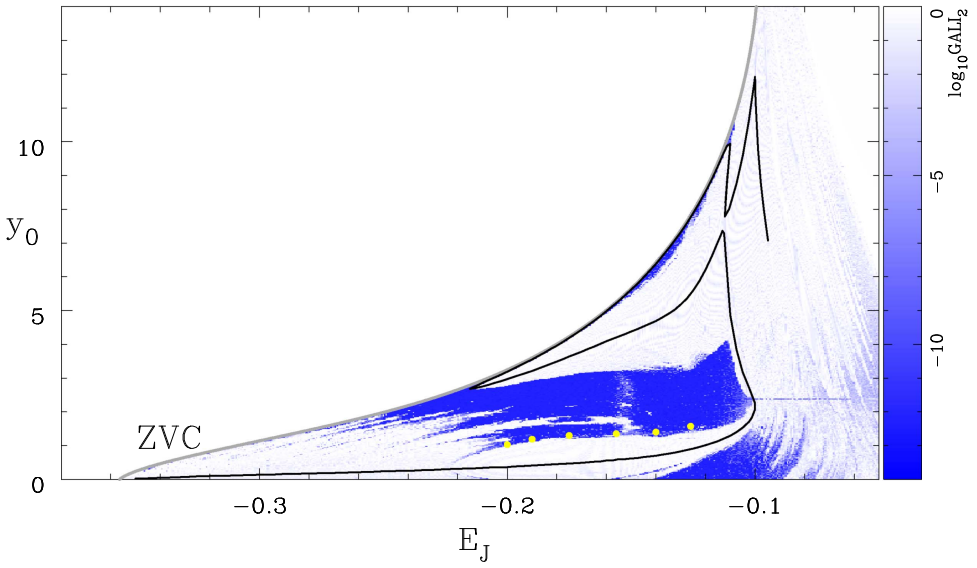

Figure 5. Chaoticity of the planar orbits on the equatorial plane of snapshot 3. The lines and colors are the same as in Figure 1, which is the corresponding figure for snapshot 2. Here we calculate $\log_{10}(GALI_2)$ for $t_2 = 10$ Gyr. The six solid light gray (yellow in the online version) dots indicate the initial conditions of the boxy orbits we present in Figure 6.

The above results point out that in order to find orbits on the equatorial plane that support boxy features in the bar of the model, we have to consider initial conditions close to the borderline between order and chaos in Figure 1. This happens not just close to a specific resonance; we find such orbits at all energies where there are x1 periodic orbits matching the size of the bar. The regions where one should look for candidate orbits supporting boxy features in the models are those that still appear white after 1 Gyr of integration in Figure 1(a) and are found to be marginally inside the chaotic region in Figure 1(b), i.e., have developed a chaotic character in time 1 Gyr $< t <$ 10 Gyr.

4.1.2. Snapshot 3, $t = 7.0$ Gyr

We repeat the same analysis for the model of snapshot 3. Figure 5, like Figure 1, gives the color-coded $\log_{10}(GALI_2)$ quantity in a (E_J, y_0) diagram, however this time only for $t_2 = 10$ Gyr. Boxy orbits are again found at the borderline between order and chaos. We present six of them in Figure 6. Their locations in Figure 5 are at (E_J, y_0) = (−0.2, 1.03), (−0.19, 1.19), (−0.175, 1.3), (−0.156, 1.35), (−0.14, 1.4), and (−0.126, 1.57). The time evolution of the quantity $\log_{10}(GALI_2)$ below each panel with the morphology of the orbit in Figure 6 implies that the presented orbits are sticky. For $t < t_1 = 1$ Gyr, these orbits can

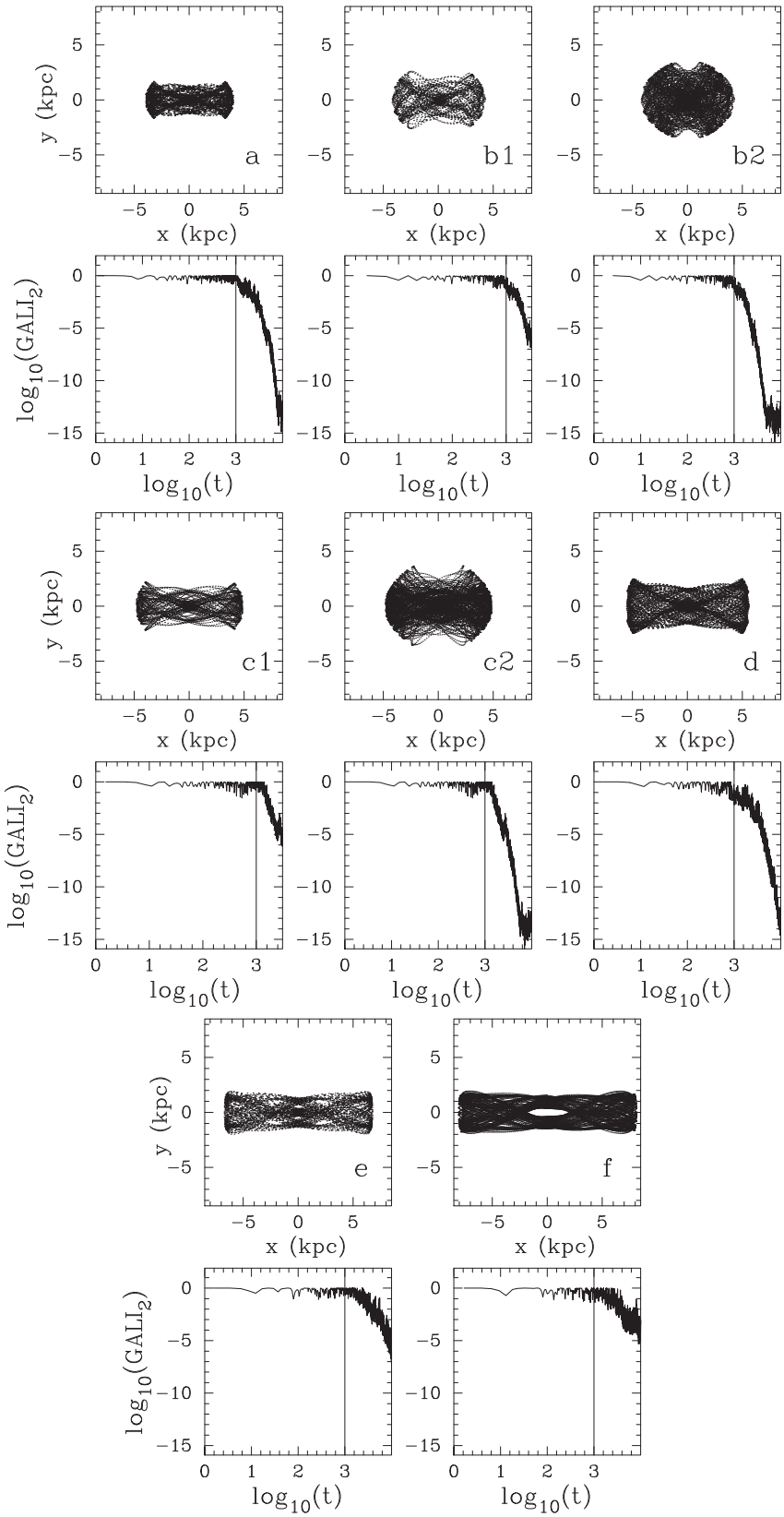

Figure 6. Six orbits with boxy character on the equatorial plane of the model of snapshot 3. Their location on the (E_J, y_0) diagram is denoted with solid light gray (yellow in the online version) dots in Figure 5. They are (a) (−0.2, 1.03), (b) (−0.19, 1.19), (c) (−0.175, 1.3), (d) (−0.156, 1.35), (e) (−0.14, 1.4), and (f) (−0.126, 1.57). For orbits in panels (b) and (c), we give their morphology in two different time windows (b1, b2 and c1, c2, respectively). All of them are sticky to the stability islands of the stable representative of the main family of periodic orbits of the system. Below each labeled panel is the corresponding $GALI_2$ index up to 10 Gyr. The vertical line indicates the location of the first Gyr.

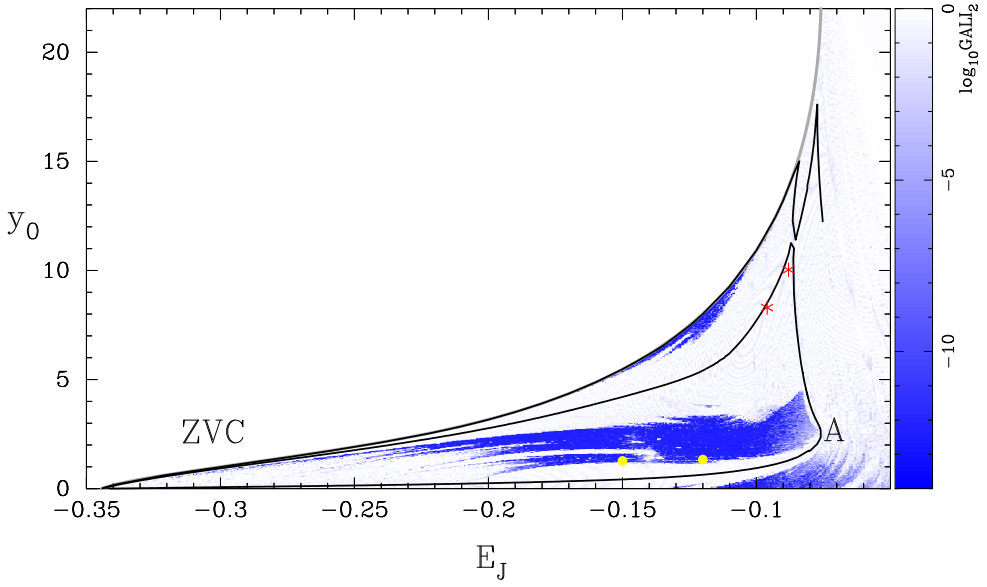

Figure 7. Chaoticity of the planar orbits on the equatorial plane of snapshot 4. The lines and colors are the same as in Figure 1. Here we calculate $\log_{10}(GALI_2)$ for $t_2 = 10$ Gyr. The two solid light gray (yellow in the online version) dots indicate the positions of orbits (a) and (b) in Figure 8, while the two asterisks indicate those of orbits (c) and (d) in the same figure.

hardly be distinguished from regular orbits. We pay special attention to the orbits of panels (b) and (c) that we present in two different time windows; they are labeled b1, b2, and c1, c2, respectively. In the first time window, which is larger than 1 Gyr, we plot the orbits for the time they retain their boxiness, while for the second one, we plot the orbits as they appear after being integrated for $t_2 = 10$ Gyr. We observe that the orbit in b1 is boxy and evidently harbors an X structure. However, within 10 Gyr, it shows a strongly chaotic character. Its morphology in the configuration space is chaotic (panel (b2)) and $GALI_2$, below it, has a steep gradient downward, reaching values close to 10^{-14}. We encounter a similar evolution in the orbit described in panels (c1) and (c2). In this case, the orbit remains confined in the configuration space for more than 3 Gyr and then expands into a larger region of the configuration space, without, however, visiting within 10 Gyr all the allowed space.

We also note that the boxy orbits presented in Figure 6 have a clear $|y_{\rm min}|$ value along the $x = 0$ axis that gives them a bow-like shape, something that has its counterpart in the shape of the N-body bar in the MM models (cf. Figure 1, third panel from left, in MM). This will be further discussed in Section 5.

4.1.3. Snapshot 4, $t = 11.2$ Gyr

Finally, we repeat the same analysis for the last snapshot of the MM paper. The color-coded (E_J, y_0) diagram for this case is shown in Figure 7. This is a very slowly rotating model with $R = 2.87$ and corotation at 22.89 kpc. As we can see, the loop of the characteristic of the central family is huge. The characteristic increases monotonically until point A and then turns backward. The branch that goes back to the left reaches the minimum E_J of the ZVC. Then, it turns back again toward corotation, being essentially on the ZVC. The loop almost closes as the two parts of the characteristic come very close at about $E_J = -0.09$. Bar-supporting orbits on the equatorial plane can be found only in the lowest branch of the characteristic, while there is a large number of almost circular and stable orbits (practically white regions for $y_0 > 5$ in Figure 7) that populate the extended disk region between the end of the bar and corotation (cf. Figure 1, right panel, in MM). Four typical orbits for this model are given in Figure 8. Their locations in the (E_J, y_0) diagram are denoted with solid light gray (yellow in the online version) dots and asterisks in Figure 7. They are at (a) (−0.15, 1.27) and (b) (−0.12, 1.33) (dots) and at (c) (−0.096, 8.292) and (d) (−0.088, 10.032) (asterisks). The accumulation of a large number of almost circular orbits for y_0 initial conditions beyond those of the bar-supporting orbits and the shape of the characteristic with the almost closed loop favor the formation of rings surrounding the bar by means of a dynamical mechanism similar to the one that led to the formation of the ring in the model of Tsigaridi & Patsis (2015).

4.2. Vertical Perturbations

Until now we have seen that a set of planar orbits with boxy morphology can be found close to the borderline between order and chaos above the characteristic of the central family of periodic orbits, as this is determined by the $GALI_2$ index in the (E_J, y_0) diagrams. Now we will examine how the morphology of these orbits changes if we perturb them vertically by adding a $p_{z_0} \neq 0$ to their initial conditions. This means that the orbits we present in this section have initial conditions y_0 and $p_{z_0} \neq 0$, as well as z_0 and $p_{y_0} = 0$. Hereafter, when we give the initial conditions of an orbit, we mean the nonzero ones, if not otherwise indicated.

For 3D orbits, their regular or chaotic character cannot be easily depicted on a single diagram, since we deal in general with four initial conditions. Considering an orbit, the monotonic variation of a single initial condition may lead to a nonmonotonic succession of regular and sticky chaotic orbits. It is not easy to know in a 4D space whether the deviation from the initial condition of a torus will bring an orbit in a chaotic sea or closer to an invariant torus around another stable periodic orbit. However, we realized that for all planar boxy orbits, when we started increasing their p_{z_0} coordinate, we could find a Δp_z range for which the 3D orbits retained their boxy character. The variation of the $GALI_2$ index with time

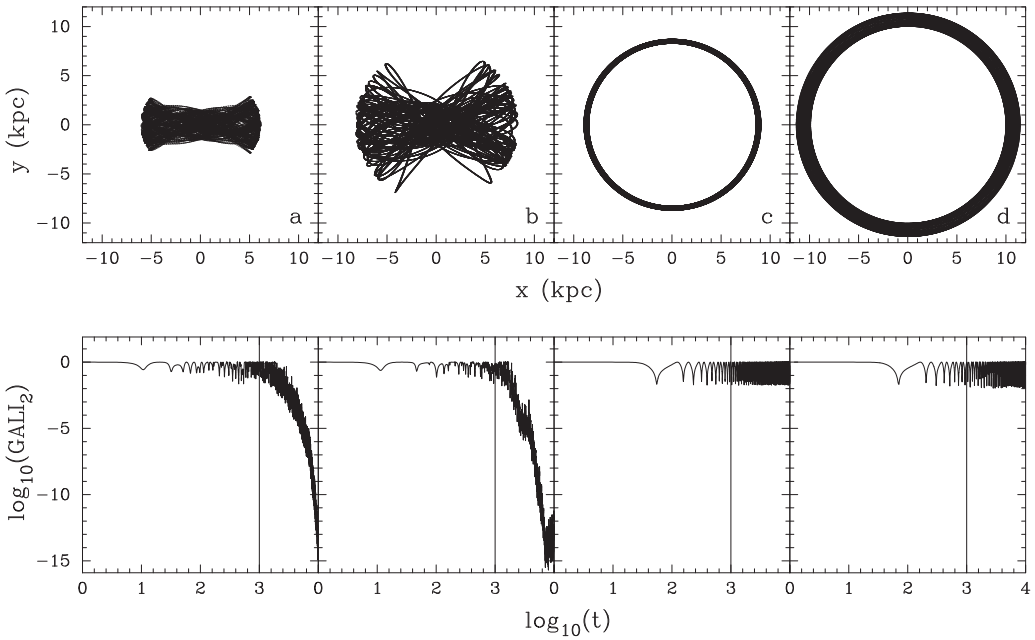

Figure 8. Four orbits on the equatorial plane of the model of snapshot 4. Their location on the (E_J, y_0) diagram is denoted with solid light gray (yellow in the online version) dots and asterisks in Figure 7. They are (a) and (b) the orbits with the dots located at (E_J, y_0) = (−0.15, 1.27) and (−0.12, 1.33), respectively, and (c) and (d) the orbits with the asterisks at (−0.096, 8.292) and (−0.088, 10.032) in Figure 7. Below each labeled panel is the corresponding $GALI_2$ index up to 10 Gyr. The vertical line indicates the time corresponding to the first Gyr.

was similar to that of the boxy 2D orbits. This led to the conclusion that the building blocks not only for 2D but also for 3D boxy structures in real galaxies can be either regular orbits on the most remote tori around stable periodic orbits or orbits sticky to them. The latter orbits are, strictly speaking, chaotic, but their sticky character keeps them confined in particular regions of the phase space for sufficiently long times. This way, they can support a given morphology.

Below, we give some typical examples of 3D boxy orbits or, in other words, orbits with three boxy projections in the configuration space. In Figure 9, we present six orbits from the model of snapshot 2. The panels of each row refer to the same orbit. A number that refers to each orbit and helps us in the description is given on the right-hand side of each row. In column (a), we give the face-on view, column (b) gives the side-on view, column (c) gives the end-on view, and column (d) gives the evolution of $GALI_2$ in a log–log plot, as in the previous figures.

In general, by starting from a planar orbit and adding p_z, we have the following possibilities: we will either reach a torus around x1, a torus around a stable 3D family bifurcated from x1, a chaotic zone between the two sets of tori, or we will enter a chaotic zone (see Patsis & Katsanikas 2014a and P. A. Patsis & M. Harsoula 2017, in preparation). The result depends both on the energy of the orbit and on the p_z initial condition. The energy will determine the available resonant families of periodic orbits existing (their number increases with E_J), while p_z will decide about the location of the orbit in the phase space. In the present paper, we are just interested in pointing out that there are vertical perturbations that support the 3D boxy character. The planar orbits we start from have to be sought along the lines we find for the 2D boxy orbits in the (E_J, y_0) diagrams. In Figure 9, the orbits in the four first rows are at the same energy we have for the (y, p_y) surface of section in Figure 2, i.e., for $E_J = -0.2$. Orbits 1 and 2 have $y_0 = 1.07$, which would be an initial condition on an invariant curve around x1 in the (y, p_y) Poincaré surface of section (Figure 2) if we had $p_z = 0$. However, orbit 1 is perturbed by $p_z = 0.15$, and orbit 2 is perturbed by $p_z = 0.2$. In both cases, the orbits form boxes in all three projections. The side-on and end-on morphologies clearly support peanut-shaped structures. The $GALI_2$ evolution of orbit 1 (panel (d)) indicates that it is a regular orbit, while that of orbit 2 points to a sticky one. The next orbit, perturbed by $p_z = 0.085$, has $y_0 = 1.24$; i.e., the (y, p_y) Poincaré surface of section in Figure 2 corresponds to the sticky orbit plotted with the solid gray/light blue consequents. Again in this case, the 3D boxy character is retained; however, this time the vertical perturbation is smaller. For the same energy, we give an example of an orbit with $y_0 = 1.19$ and $p_z = 0.165$, which is orbit 4 in Figure 9. If $p_z = 0$, the orbit would be sticky to an x1 orbit. Now it is sticky again, but its morphology clearly resembles the morphology of the x1v2 family, which is bifurcating, usually as unstable, at the vertical 2:1 resonance (Skokos et al. 2002a). This can be seen in panel (b) of row 4 in Figure 9. Strictly speaking, this side-on profile is not boxy. Nevertheless, it has a shape similar to that of the two main vertical bifurcations of x1. Considering several orbits like this in different energies will lead to a boxy profile. Orbits 5 and 6 are in nearby energies and have similar morphologies and evolution of $GALI_2$ as the previous ones. Orbit 5 is at $E_J = -0.206$ with $y_0 = 1.17$ and $p_z = 0.162$, while orbit 6 is at $E_J = -0.195$ with $y_0 = 1.19$ and $p_z = 0.15$.

An interesting result is that the sticky 3D boxy orbits in many cases harbor an X feature in their *face-on* projections (column (a)). This is conspicuous in orbits 3, 4, and 5, as well as in regular orbit 1. This is in agreement with the result of Patsis & Katsanikas (2014b), who suggested that sticky, boxy orbits in the immediate neighborhood of the vertical 2:1 resonance have embedded X features in their face-on projections. The property of stickiness was also the reason for the appearance of an X inside the bars of the 2D barred-spiral models in Tsigaridi & Patsis (2015). The same analysis

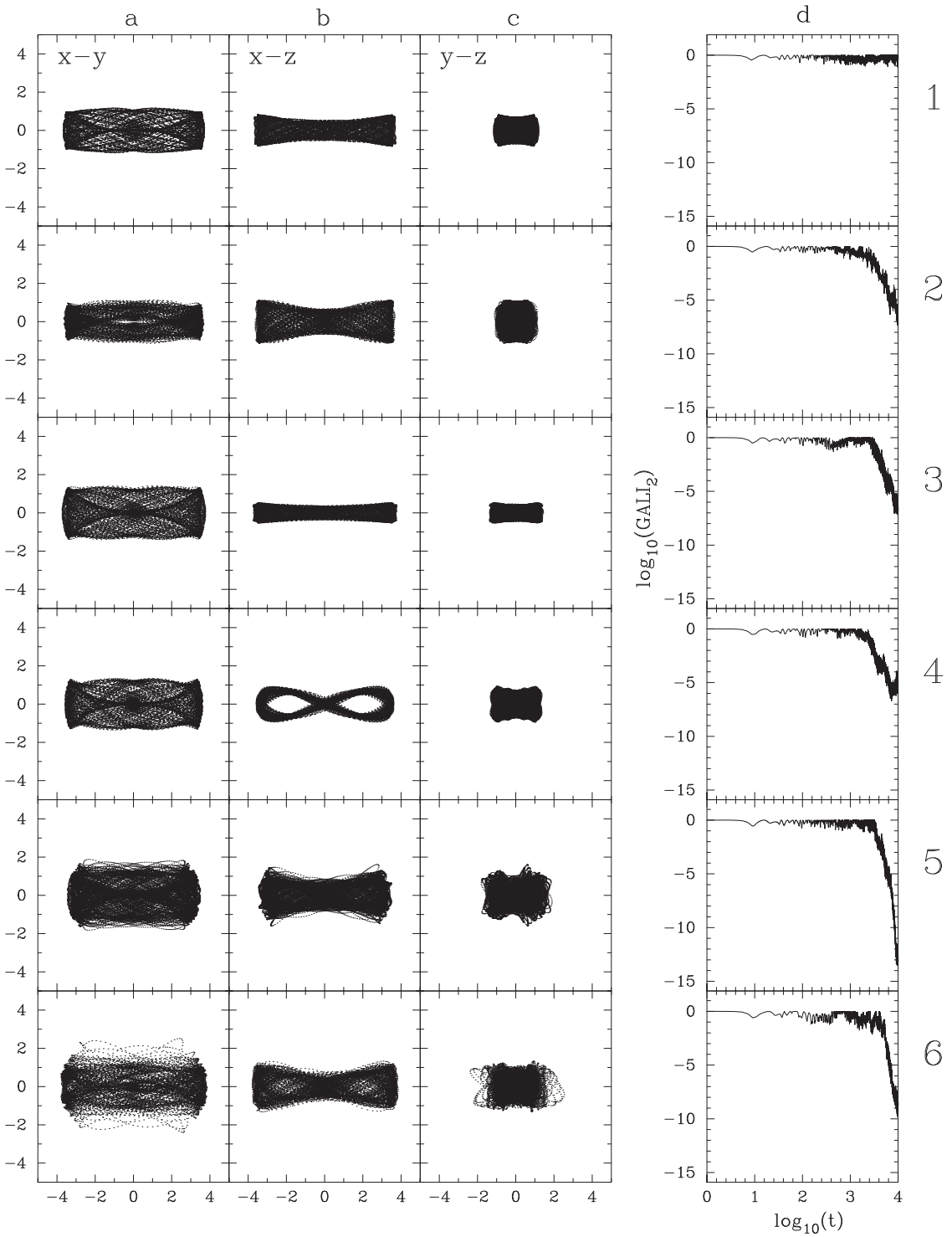

Figure 9. 3D orbits associated with 3D boxy structures in the model of snapshot 2. Orbit 4 has a side-on profile similar to x1v2 orbits, while all the rest have three boxy projections. Orbits 1, 3, 4, and 5 harbor an X feature in their face-on projections. The $GALI_2$ evolution indicates the sticky character of orbits 2 to 6, while orbit 1 is regular. The units on the axes of the first three columns are in kpc.

led to similar results in the cases of the two other models considered here as well. In Figure 10, we present some typical orbits for the model of snapshot 3. Again here, double boxiness with an X feature embedded in the boxy face-on projection is found by perturbing boxy planar orbits in the z direction by p_z. This is given in orbit 1, which is at $E_J = -0.156$, $y_0 = 1.35$, and $p_z = 0.09$. In Figure 6(d), we have given the corresponding orbit with $p_z = 0$. As orbits 2 and 3 show, the stable 3D families (x1v1 and x1v1′ in the notation of Skokos et al. 2002a) bifurcated from x1 at the vertical 2:1 resonance do exist in the model. In order to track them, we perturbed the z coordinate in the vertical direction, while we put the initial condition $p_z = 0$. The initial conditions of the two orbits are $E_J = -0.156$, $y_0 = 0.7$, and $z = 0.63$ (orbit 2) and $E_J = -0.156$, $y_0 = 0.7$, and $z = -0.63$ (orbit 3). Their morphology indicates that they belong to invariant tori in the

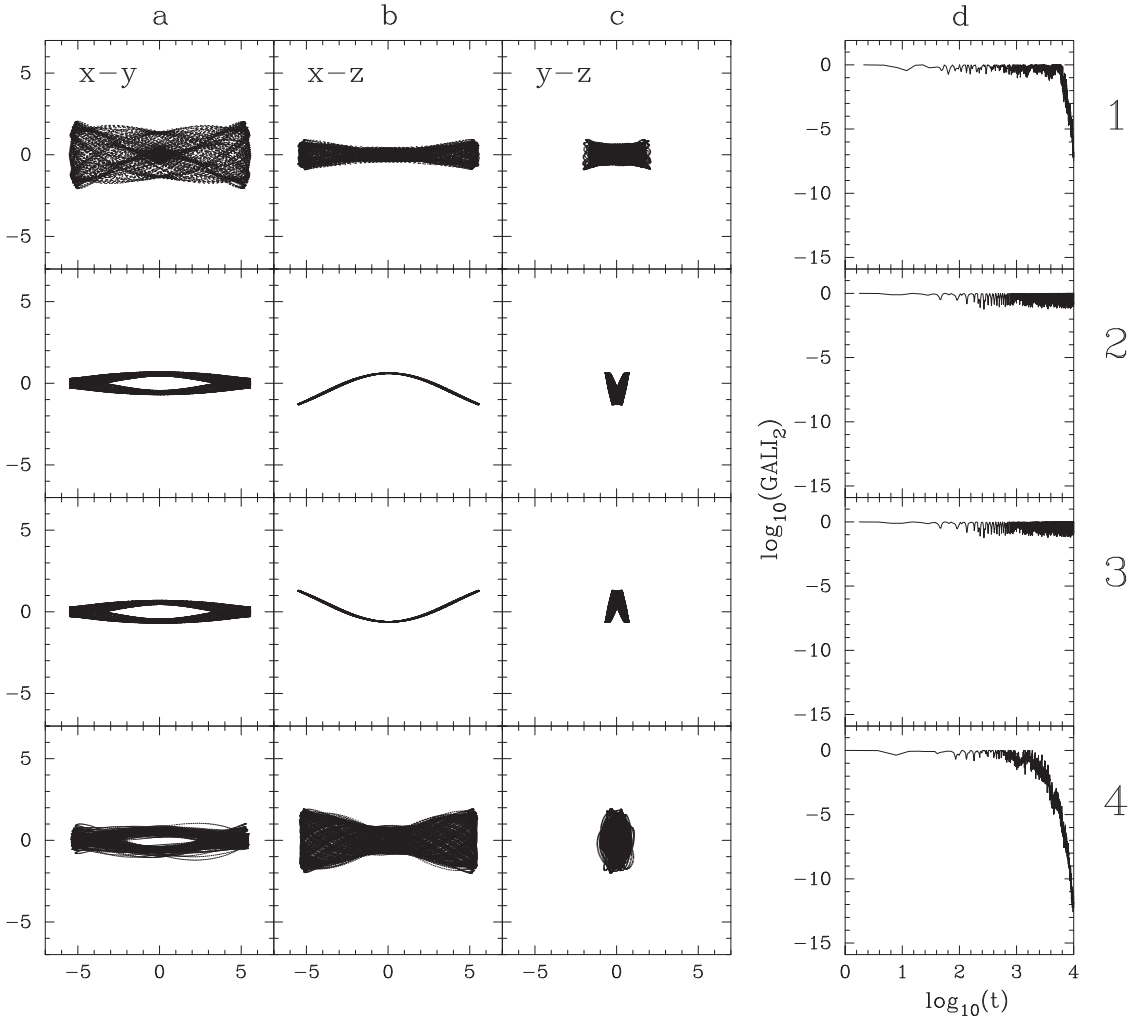

Figure 10. Orbits in the model of snapshot 3. Orbit 1 is a sticky orbit with a boxy 3D structure and an X feature embedded in the face-on projection, orbits 2 and 3 are frown and smile regular 3D orbits on x1v1 tori, and orbit 4 is a sticky orbit that changes its face-on elliptical morphology, becoming boxy as soon as it abandons its regular behavior. The units on the axes of the first three columns are in kpc.

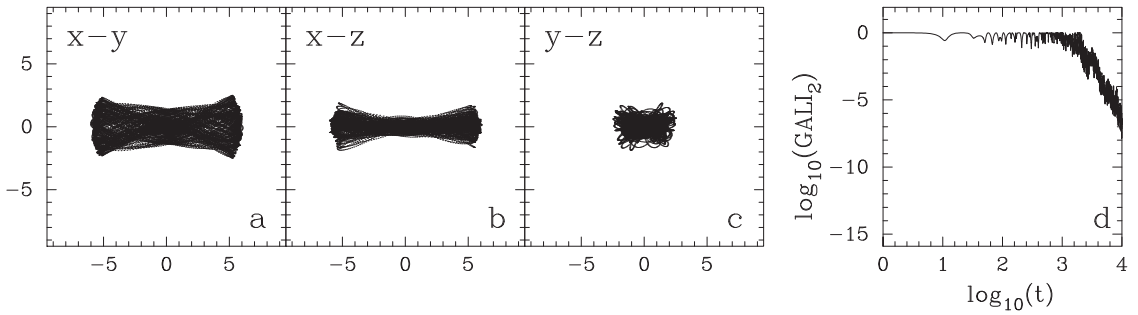

Figure 11. A 3D boxy orbit in the model of snapshot 4. It is sticky (panel (d)) and reproduces the X feature in its face-on projection (panel (a)). The units on the axes of the first three panels are in kpc.

immediate neighborhood of x1v1 (Patsis & Katsanikas 2014b). This is consistent with the evolution of their $GALI_2$ index in panel (d). By means of such orbits, we can construct a sharp X-shaped side-on profile with, however, an elliptical face-on morphology. A nice example is given by orbit 4, with nonzero initial conditions $E_J = -0.156$, $y_0 = 0.7$, and $p_z = 0.303$. This is a sticky orbit (see panel (d)). As long as it has a regular character, the orbit supports an elliptical face-on morphology. However, when it starts diffusing in the configuration space, it tends to obtain a boxy structure (panel (a)).

Finally, in Figure 11, we give an example of an orbit from the model of snapshot 4 that reproduces the main morphology we want to underline that exists in our models. Namely, it is a sticky orbit with all its projections boxy, while in its face-on projection, it has a discernible X feature. The initial conditions of the orbit are $E_J = -0.15$, $y_0 = 1.27$, and $p_z = 0.07$.

The process for finding 3D double boxy orbits by perturbing 2D boxy ones can be applied at all energies, for which we could find x1 orbits supporting the size of the N-body bar in the models. However, as E_J increases and we approach corotation,

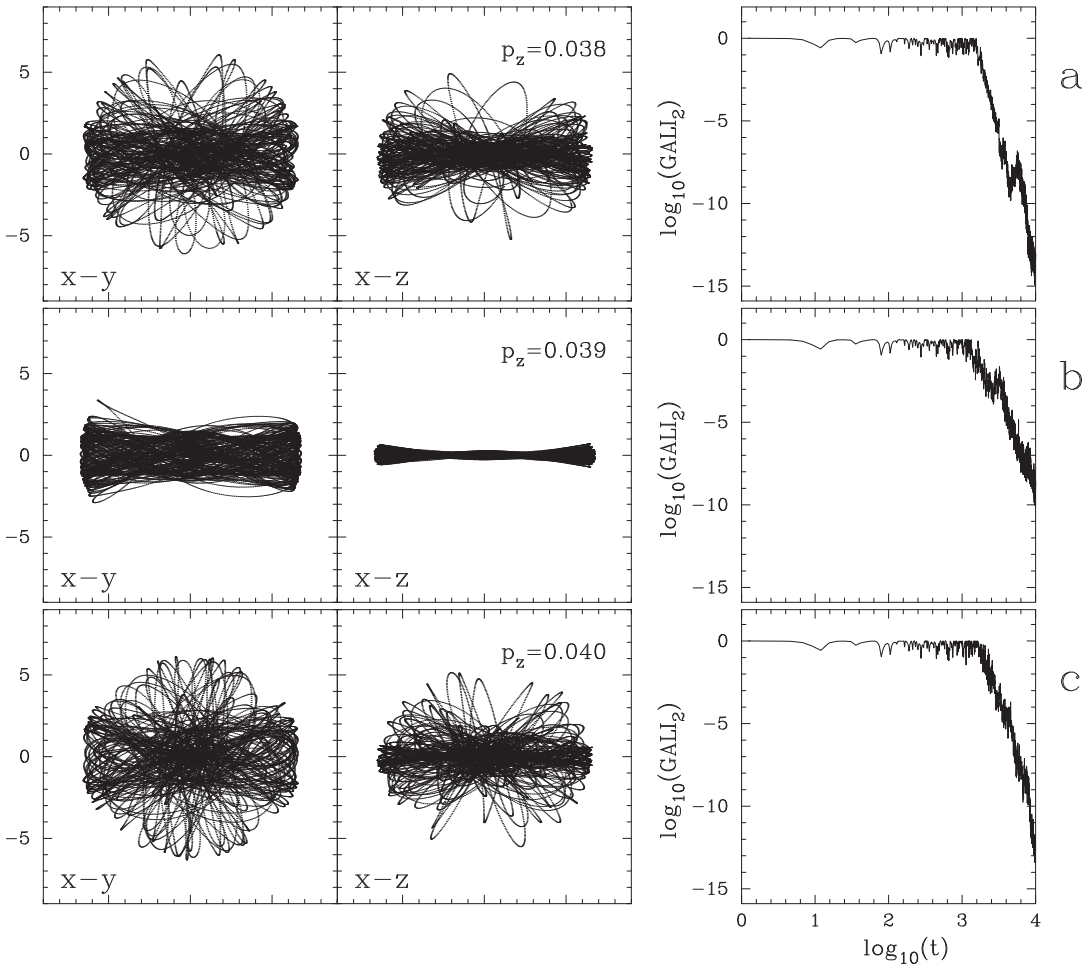

Figure 12. Planar orbit presented in Figure 6(e) perturbed by $p_z = 0.038$ (a), 0.039 (b), and 0.040 (c). In panels (a) and (c), the orbits diffuse in configuration space, while in panel (b), the orbit has a double boxy character for more than 3 Gyr.

the structure of phase space becomes more complicated, due to the presence of more families of periodic orbits introduced in the system at successive resonances (Skokos et al. 2002a). The monotonic variation of an initial condition (e.g., p_z) may lead either to quasi-periodic orbits around stable periodic orbits and the chaotic orbits sticky to them or to direct diffusion in the chaotic sea. This happens, in general, in a nonmonotonic way. As an example, in Figure 12, we give the orbit of the model of snapshot 3 with $(E_J, y_0) = (-0.14, 1.4)$, given in Figure 6(e), perturbed by $p_z = 0.038$, 0.039 and 0.040. We observe that, for $p_z = 0.038$, the orbit clearly diffuses in the configuration space; for $p_z = 0.039$, it has a double boxy character for more than 3 Gyr before starting to diffuse in the chaotic sea (the quantity $\log_{10}(\mathrm{GALI}_2) \lessapprox -10$ at $t = 10$ Gyr); and, for $p_z = 0.040$, we again have a practically chaotic orbit.

In order to demonstrate the fact that at energies where several families of 3D periodic orbits coexist, different perturbations of the planar orbits may lead us to different boxy configurations, we present in Figure 13 the planar orbit of the model of snapshot 2 given in Figure 4(e). It has $(E_J, y_0) = (-0.162, 1.27)$. In panel (a), $p_z = 0.016$. The orbit, being initially boxy on the equatorial plane, has a narrow side-on profile. This morphology lasts for more than 3 Gyr. Then, the orbit occupies a larger volume in phase space. However, it retains a less confined but boxy character in its face-on view, while in the side-on view, its morphology resembles that encountered in orbits close to the stable "frown" and "smiles" periodic orbits. For $p_z = 0.032$ (Figure 13(b)), the orbit remains boxy in its face-on view for an even longer time than that for $p_z = 0.016$, but then it diffuses in phase space and does not have any particular morphology in either projection. The side-on views of the orbits in both cases of Figure 13 clearly indicate that they have been trapped close to an x1v3 periodic orbit, which is bifurcated at the 3:1 vertical resonance (Patsis et al. 2002). It is worth underlining that the side-on profiles of the double boxy orbits in which a morphology of a higher-order n: 1 resonance may be identified are, in general, narrower as we approach corotation, in agreement with the profile of the corresponding periodic orbits found in Patsis et al. (2002).

Before closing, we want to add a comment on the general morphology of the three models from the MM simulation, especially the one that appears in snapshots 3 and 4 (cf. Figure 1 in MM). This morphology is that of a bar surrounded by a ring, with the areas on the sides of the bar being rather depleted from particles. Beyond this central structure, there is a disk without any special feature. The bar and ring morphology could easily correspond to that of a bar with an inner ring (Buta & Combes 1996). However, in this particular case, corotation is far away, so the question that arises is: what is the orbital content behind this structure in the model? The orbits that we have presented so far support a bar of the size of the bars in the MM N-body snapshots. The folding of the characteristic

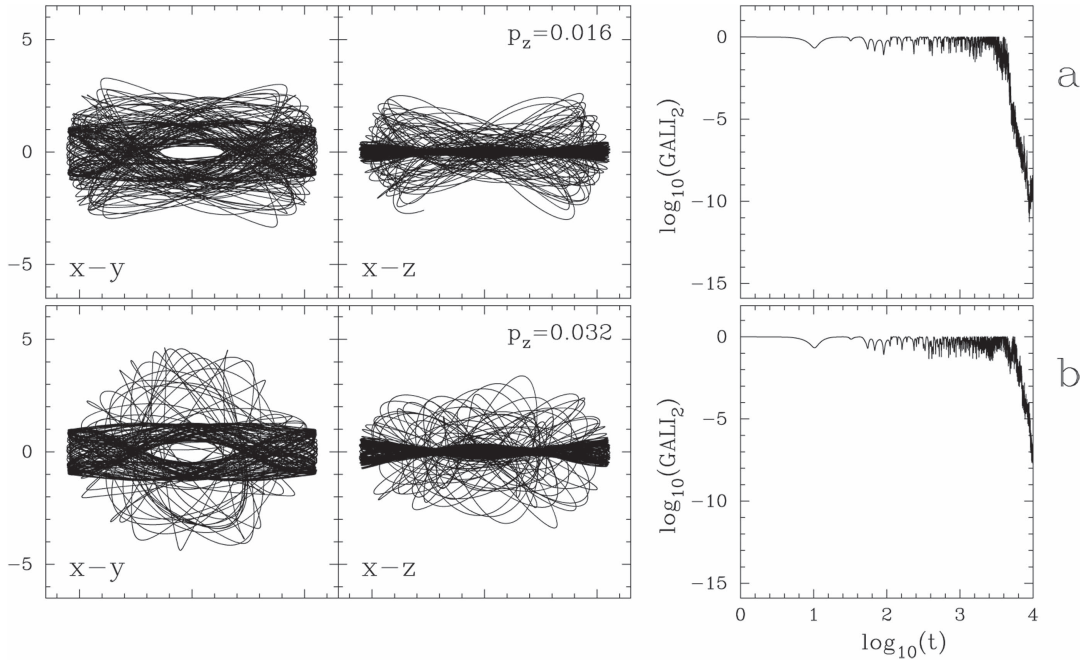

Figure 13. Planar orbit presented in Figure 4(e), $(E_J, y_0) = (-0.162, 1.27)$, perturbed by $p_z = 0.016$ (a) and $p_z = 0.032$ (b). The orbit initially has a x1v3 side-on profile, while for longer times, its morphology is different in each case.

provides appropriate round orbits with the right dimensions to support the ring.

Focusing on the model of snapshot 4, we can see that the sticky bar-supporting orbits have face-on projections that reinforce a bar structure with two minima along the minor axis, giving it a bow-like or peanut-like form, but on the equatorial plane of the model in this case (Figure 11(a)). The planar, sticky, boxy orbits have a similar shape (Figure 8(a)). The corresponding MM model has this morphological feature as well. At larger energies, one can find in the plane some tumbling bar-supporting orbits (see Figure 8(b)). However, even when considering these orbits to be among those that populate the model, the areas on the sides of the bar remain rather empty. Finally, not only the presence of the circular orbits with the right dimensions, but also the regression of the characteristic and the following continuation of the curve forward, i.e., toward corotation, favor the accumulation of round orbits around the bar. This folding of the characteristic brings into the system twice as many stable circular periodic orbits as in the rest of the energies, and this supports the formation of a circular ring at a certain distance. All of these are summarized in Figure 14, where we combine the orbits of Figure 8 in order to reproduce the main morphology of the *N*-body MM model. We also plot two circular periodic orbits as a reference to the dimensions of the ring. The initial conditions for the two periodic orbits are $E_J = -0.0961538$, $y_0 = 8.49173$ and $E_J = -0.0898683$, $y_0 = 10.0141$, respectively. Figure 14 is by no means the result of a self-consistent Schwarzschild-type model. It just shows that in the snapshot 4 model, there are orbits that can reproduce the morphology of the corresponding MM *N*-body model.

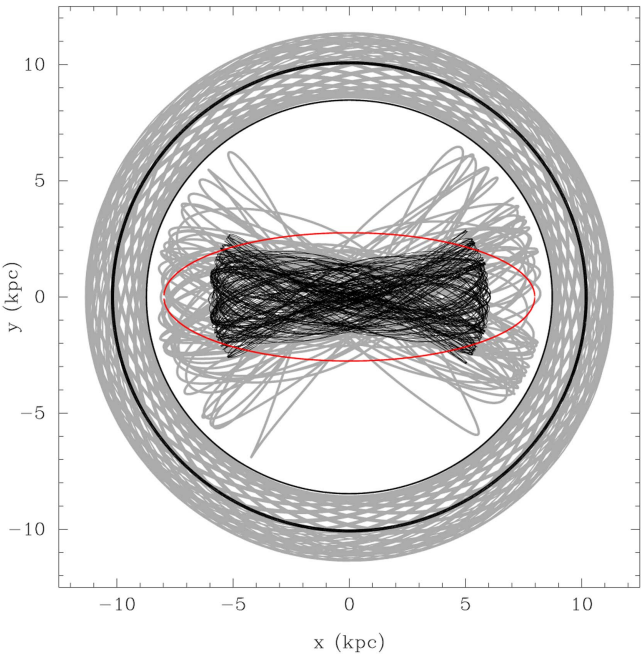

Figure 14. The set of four nonperiodic orbits of the model for snapshot 4 that are depicted in Figure 8 reproduce the basic morphological features of the corresponding MM model. Two circular periodic orbits at close-by energies are also plotted. A ringed bar morphology is formed, but away from corotation, which in this case is at 22.89 kpc. The red ellipse indicates the bar in the MM snapshot.

4.3. Fast-rotating Bars

In the present paper, we study orbital boxiness in the MM models, all of which have slow-rotating bars. We have found that boxiness is a property associated with the presence of x1 orbits supporting the bar. This is not related to the pattern speed of the model per se. However, in slow-rotating models like those of the MM simulations, there are a lot of non-bar-supporting orbits between the end of the bar and corotation. These are the circular orbits. Contrarily, in fast-rotating bars, one can find bar-supporting elliptical x1 orbits almost all the way from the center of the system to corotation.

In order to examine the dependence of the results on the pattern speed, a systematic study with models of bars rotating in a range of Ω_b is needed. This is not done in the present paper. Nevertheless, we considered the potential of one of the models (model of snapshot 3) with a higher pattern speed, so that we obtained a ratio $R_{\rm CR}/\alpha_b = 1.1$. This model is not the result of an *N*-body simulation. It has been used just for studying the orbital behavior of bar-supporting orbits close to corotation.

We found again in this case that the 2D orbits at the borders of the stability islands of x1 were boxy, and we could find 3D boxy orbits by perturbing them in the vertical directions within a certain Δp_z range. So the rule, in principle, also applies in the case of bar-supporting orbits close to corotation. However, we have to note that the planar, boxy bar-supporting orbits we could find close to corotation on the plane were like orbit 1 in Figure 3 and not like orbit 3 of the same figure. In other words, at their apocentra, the segments that were parallel to the minor axis of the bar were relatively small. On the (y, p_y) Poincaré sections, we found more islands of orbits of higher multiplicity than in Figure 2. Many of them surround the stability islands of x1, and this affects the shape of the sticky orbits in the region. Also, the Δp_z range for which we could find double boxy orbits was much smaller. The 3D double boxy bar-supporting orbits remained confined close to the equatorial plane. We could find orbits with boxy edge-on profiles away from the equatorial plane, but their face-on projections did not support the bar.

In conclusion, the mechanism applies independently of the pattern speed value. However, it applies more efficiently away from corotation. If a bar stops away from corotation (as in the slow-rotating models), then almost all of it can be considered a double boxy structure. In fast-rotating models, the 3D double boxy part can be found pronounced in the inner parts of the bar.

5. Discussion and Conclusions

The orbital analysis we present in this paper suggests a recipe for building 2D and 3D boxy structures in rotating bars. The basic idea is as follows. Let us start with the planar backbone of periodic orbits for building a bar, namely with the well-known x1 family. However, instead of populating the model with regular quasi-periodic orbits encountered in the immediate neighborhood of the periodic orbit, we consider either periodic orbits close to the last KAM or, more efficiently, the sticky orbits that surround the islands of stability, as they appear in the surfaces of the section. The selection of these orbits secures a boxy morphology on the plane.

In a 3D model, when we eject particles that follow the 2D boxy orbits out of the plane by adding a $p_z \neq 0$ perturbation, we find that there is always a Δp_z range of perturbations for which all three projections of the 3D orbits are boxy. A remarkable property of these sticky boxy orbits is the formation of an X feature embedded in the bar in the face-on projections.

In several cases, the side-on views had a peanut-shaped morphology. However, it is beyond the scope of the present paper to attribute specific orbits or sets of orbits to the observed peanut shapes encountered in edge-on galaxies or snapshots of *N*-body models. This was investigated thoroughly in Patsis & Katsanikas (2014b). In this study, we emphasize that as long as we have the usual ellipses of the x1 family (or the x1-tree in 3D models according to Skokos et al. 2002a) in a rotating bar, we can find a class of boxy 2D and 3D orbits. They are sticky chaotic orbits, as their $\rm GALI_2$ index indicates, and they can support the bar or a part of the bar for many Gyr.

Observational features that can be reproduced by using such orbits as building blocks can first be the boxy- or peanut-shaped bulges in the central parts of the bars. In these cases, in the face-on views of the galaxies, we will observe boxy isophotes in their central parts, inside the bar, as in the sample of galaxies presented by Erwin & Debattista (2013). Furthermore, the present study indicates that in cases of slow-rotating bars, as in the MM models, the 3D boxy structure may constitute a major part of the bar. The presence of the X feature in the face-on views of the orbits, as well as the presence of a ring surrounding the bar, raises the question of whether a dynamical mechanism such as the one proposed by Tsigaridi & Patsis (2015) acts in galaxies like IC 5240, presented in Buta et al. (2007).

In closing, we enumerate our conclusions.

1. In models where the family of x1 ellipses exists in the MM models, we can find a class of sticky chaotic orbits with a 2D and/or 3D boxy structure. The shapes of these orbits, after integrating them for 10 Gyr and the evolution of their $\rm GALI_2$ index, show that they can be used as building blocks for structures that last for several Gyr. They exist in a large range of E_J values.
2. 2D nonperiodic boxy orbits can be found on the outermost invariant curves around x1 on a surface of section or in regions in the immediate neighborhood of the stability islands. We find them for all E_J values, for which we encounter x1 periodic orbits that do not exceed the size of the *N*-body bar.
3. For finding 3D orbits with boxy morphology in both face-on and edge-on views, one has to perturb the boxy planar orbits in the vertical direction. There is always a Δp_z interval in the initial conditions of the perturbed, initially planar orbits in which the 3D orbits will have a boxy structure. These are 3D sticky chaotic orbits. Their face-on projections are different from those of the quasi-periodic orbits close to x1 and its 3D bifurcations at all E_J values we find them.
4. In the *face-on* projections of these sticky boxy orbits, we find the formation of an X embedded in the boxy structure.
5. Such orbits can be used to construct models with boxy isophotes inside the face-on views of the bars. The areas of the boxy isophotes in these cases correspond to the extent of the edge-on boxy bulges, in agreement with the results of Patsis & Katsanikas (2014b).
6. According to our analysis, the degree of boxiness of a bar, or of a part of it, indicates which orbits are populated. If quasi-periodic orbits in the immediate neighborhood of the periodic orbits of the central family prevail, the face-on projections will be elliptical. In contrast, if the majority of the nonperiodic orbits building the bar or its part are at the edges of the stability islands and/or sticky chaotic orbits next to them, then the supported shape in the face-on views will be boxy. In both cases, we can have boxy edge-on profiles.
7. In the case of slow rotation, our 3D sticky, boxy orbits can build boxy bars (not just boxy features embedded in the bars). In such cases, almost the whole bar is boxy. The slow rotation of the models favors the appearance of a ringed bar morphology, despite the fact that corotation is at large distances.

We note that, in a fast-rotating case we examined, we found that boxy bar-supporting planar orbits close to

corotation had small segments parallel to the minor axis of the bar at their apocentra. By perturbing them in the vertical direction, we could find boxy orbits supporting the bar confined close to the equatorial plane. In such a case, double boxy structures are found mainly embedded in the bar.

L.C.V. and I.P. thank the Mexican Foundation CONACYT for grants that supported this research. L.C.V. thanks the Research Center for Astronomy (RCAAM) of the Academy of Athens for its hospitality during his visit there, when part of this work was completed. This work is part of the project "Study of stellar orbits and gravitational potentials in galaxies, with numerical and observational methods," in which researchers from RCAAM and INAOE participate. Ch.S. acknowledges support by the National Research Foundation of South Africa (Incentive Funding for Rated Researchers, IFRR) and also thanks RCAAM for its hospitality during his visits there in order to collaborate with P.A.P. and L.C.V. We acknowledge fruitful discussions with G. Contopoulos and L. Athanassoula.

References

Athanassoula, E. 1992a, MNRAS, 259, 328
Athanassoula, E. 1992b, MNRAS, 259, 345
Barazza, F. D., Jogee, S., & Marinova, I. 2008, ApJ, 675, 1194
Benettin, G., Galgani, L., Giorgilli, A., & Strelcyn, J.-M. 1980, Mecc, 15, 21
Binney, J., & Tremaine, S. 2008, Galactic Dynamics (2nd ed.; Princeton, NJ: Princeton Univ. Press)
Bountis, T., & Papadakis, K. E. 2009, CeMDA, 104, 205
Buta, R., & Combes, F. 1996, Fund. Cosmic Phys., 17, 95
Buta, R. J., Corwin, H. G., & Odewahn, S. C. 2007, The de Vaucouleurs Altlas of Galaxies (Cambridge: Cambridge Univ. Press)
Capuzzo-Dolcetta, R., Leccese, L., Merritt, D., & Vicari, A. 2007, ApJ, 666, 165
Carpintero, D. D., Muzzio, J. C., & Navone, H. D. 2014, MNRAS, 438, 2871
Contopoulos, G. 1980, A&A, 81, 198
Contopoulos, G., & Grosbol, P. 1989, A&ARv, 1, 261
Contopoulos, G., & Harsoula, M. 2008, IJBC, 18, 2929
Contopoulos, G., & Harsoula, M. 2013, MNRAS, 436, 1201
Contopoulos, G. 2002, Order and Chaos in Dynamical Astronomy (Berlin: Springer)
Debattista, V. P., & Sellwood, J. A. 2000, ApJ, 543, 704
Dehnen, W. 1993, MNRAS, 265, 250
Erwin, P., & Debattista, V. P. 2013, MNRAS, 431, 3060
Eskridge, P. B., Frogel, J. A., Pogge, R. W., et al. 2000, AJ, 119, 536
Ferrers, N. M. 1877, QJPAM, 14, 1
Harsoula, M., & Kalapotharakos, C. 2009, MNRAS, 394, 1605
Harsoula, M., Kalapotharakos, C., & Contopoulos, G. 2010, in ASP Conf. Ser. 424, 9th Int. Conf. Hellenic Astronomical Society, ed. K. Tsinganos, D. Hatzidimitriou, & T. Matsakos (San Francisco, CA: ASP), 377
Kaufmann, D. E., & Contopoulos, G. 1996, A&A, 309, 381
Knapen, J. H., Shlosman, I., & Peletier, R. F. 2000, ApJ, 529, 93
Machado, R. E. G., & Athanassoula, E. 2010, MNRAS, 406, 2386
Machado, R. E. G., & Manos, T. 2016, MNRAS, 458, 3578
Manos, T., & Athanassoula, E. 2011, MNRAS, 415, 629
Manos, T., Bountis, T., & Skokos, C. 2013, JPhA, 46, 254017
Manos, T., & Machado, R. E. G. 2014, MNRAS, 438, 2201
Manos, T., Skokos, C., & Antonopoulos, C. 2012, IJBC, 22, 1250218
Manos, T., Skokos, C., Athanassoula, E., & Bountis, T. 2008, in Nonlinear Phenomena in Complex Systems, 11, 171
Marinova, I., & Jogee, S. 2007, ApJ, 659, 1176
Menéndez-Delmestre, K., Sheth, K., Schinnerer, E., Jarrett, T. H., & Scoville, N. Z. 2007, ApJ, 657, 790
Miyamoto, M., & Nagai, R. 1975, PASJ, 27, 533
Muzzio, J. C., Carpintero, D. D., & Wachlin, F. C. 2005, CeMDA, 91, 173
Patsis, P. A., Athanassoula, E., & Quillen, A. C. 1997, ApJ, 483, 731
Patsis, P. A., Kalapotharakos, C., & Grosbøl, P. 2010, MNRAS, 408, 22
Patsis, P. A., & Katsanikas, M. 2014a, MNRAS, 445, 3525
Patsis, P. A., & Katsanikas, M. 2014b, MNRAS, 445, 3546
Patsis, P. A., Skokos, C., & Athanassoula, E. 2002, MNRAS, 337, 578
Reese, A. S., Williams, T. B., Sellwood, J. A., Barnes, E. I., & Powell, B. A. 2007, AJ, 133, 2846
Sándor, Z., Érdi, B., Széll, A., & Funk, B. 2004, CeMDA, 90, 127
Skokos, C. 2001, JPhA, 34, 10029
Skokos, C. 2010, LNP, 790, 63
Skokos, C., Antonopoulos, C., Bountis, T. C., & Vrahatis, M. N. 2003, PThPS, 150, 439
Skokos, C., Antonopoulos, C., Bountis, T. C., & Vrahatis, M. N. 2004, JPhA, 37, 6269
Skokos, C., Bountis, T., & Antonopoulos, C. 2008, EPJST, 165, 5
Skokos, C., Bountis, T. C., & Antonopoulos, C. 2007, PhyD, 231, 30
Skokos, C., Gottwald, G. A., & Laskar, J. 2016, Chaos Detection and Predictability (Berlin: Springer)
Skokos, C., & Manos, T. 2016, LNP, 915, 129
Skokos, C., Patsis, P. A., & Athanassoula, E. 2002a, MNRAS, 333, 847
Skokos, C., Patsis, P. A., & Athanassoula, E. 2002b, MNRAS, 333, 861
Soulis, P., Bountis, T., & Dvorak, R. 2007, CeMDA, 99, 129
Tsigaridi, L., & Patsis, P. A. 2015, MNRAS, 448, 3081
Voglis, N., Harsoula, M., & Contopoulos, G. 2007, MNRAS, 381, 757
Voyatzis, G. 2008, ApJ, 675, 802
Wozniak, H. 1994, in Ergodic Concepts in Stellar Dynamics, ed. V. G. Gurzadyan & D. Pfenniger (Berlin: Springer), 264
Wozniak, H., & Pfenniger, D. 1999, CeMDA, 73, 149